Implementation of the multiconfiguration time-dependent Hatree-Fock method for general molecules on a multiresolution Cartesian grid

Ryohto Sawada,[1,2] Takeshi Sato,[2,3] and Kenichi L. Ishikawa[2,3]

[1]*Department of Applied Physics, Graduate School of Engineering, The University of Tokyo, 7-3-1 Hongo, Bunkyo-ku, Tokyo 113-8656, Japan*

[2]*Photon Science Center, Graduate School of Engineering, The University of Tokyo, 7-3-1 Hongo, Bunkyo-ku, Tokyo 113-8656, Japan*

[3]*Department of Nuclear Engineering and Management, Graduate School of Engineering, The University of Tokyo, 7-3-1 Hongo, Bunkyo-ku, Tokyo 113-8656, Japan*

(Received 24 December 2015; published 29 February 2016)

We report a three-dimensional numerical implementation of the multiconfiguration time-dependent Hartree-Fock method based on a multiresolution Cartesian grid, with no need to assume any symmetry of molecular structure. We successfully compute high-harmonic generation of H_2 and H_2O. The present implementation will open a way to the first-principles theoretical study of intense-field- and attosecond-pulse-induced ultrafast phenomena in general molecules.

DOI: 10.1103/PhysRevA.93.023434

I. INTRODUCTION

The dynamics of atoms and molecules under intense (typically, $\gtrsim 10^{14}$ W/cm^2) laser pulses is of great interest in a variety of fields such as attosecond science and high-field physics [1–3], with a goal to directly measure and manipulate electronic motion. Numerical simulations of such electron dynamics are a challenging task [4]. Direct solution of the time-dependent Schrödinger equation (TDSE) cannot be applied beyond He, H_2, and Li due to a prohibitive computational cost. Thus, one of the major recent directions attracting increasing interest is the multiconfiguration self-consistent-field (MCSCF) approach, which expresses the total wave function $\Psi(t)$ as a superposition [5–9]

$$|\Psi(t)\rangle = \sum_J c_J(t)|J\rangle \tag{1}$$

of Slater determinants $|I\rangle$ built from the spin orbitals $|\phi_{(i,\sigma)}\rangle = |\phi_i\rangle \otimes |\sigma\rangle$, where $\{\phi_i\}$ and $\sigma \in \{\alpha,\beta\}$ denote one-electron spatial orbital functions and spin eigenfunctions, respectively. Different variants with this ansatz have recently been actively developed [4].

The time-dependent configuration-interaction (TDCI) methods take the orbital functions to be time independent and propagate only CI coefficients $c_I(t)$. Greenman *et al.* [10] have implemented its simplest variant, i.e., the time-dependent configuration-interaction singles (TDCIS) method, to treat atomic high-field processes. In this method, only up to single-orbital excitation from the Hartree-Fock (HF) ground state is included. Bauch *et al.* [11] have recently developed TD generalized-active-space CI based on a general CI truncation scheme and discussed its numerical implementation for atoms and diatomic molecules.

In the other class of MCSCF approaches, not only CI coefficients but also orbital functions are varied in time. The multiconfiguration time-dependent Hartree-Fock (MCTDHF) method [12,13] considers all the possible electronic configurations for a given number of spin orbitals. As its flexible generalizations, we have recently formulated the TD complete-active-space self-consistent field (TD-CASSCF) [8] and TD occupation-restricted multiple-active space (TD-ORMAS) [9] methods. The latter is valid for general MCSCF wave functions with arbitrary CI spaces [4,14], including, e.g., the TD restricted-active-space self-consistent-field (TD-RASSCF) theory developed by Miyagi and Madsen [15]. Numerical implementations of MCTDHF for atoms as well as diatomic molecules have been reported for the calculation of valence and core photoionization cross sections [16]. We have also implemented TD-CASSCF for atoms by expanding orbital functions with spherical harmonics and successfully computed high-harmonic generation and nonsequential double ionization of Be [17].

Practically, all the existing implementations are intended for atoms and diatomic molecules, exploiting the underlying symmetries with either the spherical [18–22], cylindrical [23–26], or prolate spheroidal [27–30] coordinates.

In this study, we report a three-dimensional (3D) numerical implementation of MCTDHF based on a multiresolution Cartesian grid, with no need to assume any symmetry of molecular structure; this can, in principle, be applied to any molecule. With the use of a multiresolution finite-element representation of orbital functions, we can fulfill a high degree of refinement near nuclei and, at the same time, a simulation domain large enough to sustain departing electrons. As demonstrations, we successfully compute high-harmonic generation (HHG) from H_2 and H_2O. The present implementation will open a way to the first-principles theoretical study of intense-field- and attosecond-pulse-induced ultrafast phenomena in general molecules.

This paper is organized as follows. In Sec. II, we briefly summarize the MCTDHF method. Section III describes the multiresolution Cartesian grid. Section IV explains the numerical procedure that we implement. In Sec. V, we show examples of simulation results for He, H_2, and H_2O. Conclusions are given in Sec. VI. Atomic units are used throughout unless otherwise stated.

II. MCTDHF

In the MCTDHF method [12,13], the sum in Eq. (1) runs over the complete set of $\binom{M}{N_\alpha}\binom{M}{N_\beta}$ Slater determinants $|J\rangle$ that can be constructed from N_α electrons with spin projection α, N_β electrons with spin projection β, and M spatial orbitals.

Their spin projection is consequently restricted to $S_z = (N_\alpha - N_\beta)/2$.

Let us consider a Hamiltonian in the length gauge,

$$H(t) = H_1(t) + H_2, \tag{2}$$

$$H_1(t) = \sum_{i=1}^{N}\left(-\frac{\nabla_i^2}{2} - \sum_a \frac{Z_a}{|\mathbf{x}_i - \mathbf{X}_a|} + \mathbf{x}_i \cdot \mathbf{E}(t)\right), \tag{3}$$

$$H_2 = \sum_{i=1}^{N}\sum_{j=1}^{i-1}\frac{1}{|\mathbf{x}_i - \mathbf{x}_j|}, \tag{4}$$

where $N = N_\alpha + N_\beta, X_a$ and Z_a are the charge and position of the ath atom, respectively, and $\mathbf{E}$(t) is the laser electronic field. One can derive the equations of motion for the CI coefficients $c_J(t)$ and spatial orbital functions $\phi_i(t)$, resorting to the time-dependent variational principle [31–33],

$$\delta\left(\int_{t_1}^{t_2}\langle\Psi|H(t) - i\partial_t|\Psi\rangle dt\right) = 0, \tag{5}$$

with additional constraints for uniqueness [12],

$$\langle\phi_j|\phi_k\rangle = \delta_{j,k}, \quad \left\langle\phi_j\left|\frac{\partial\phi_k}{\partial t}\right.\right\rangle = 0. \tag{6}$$

The equations of motion are

$$i\dot{c}_J = \sum_K \langle J|H(t)|K\rangle c_K \tag{7}$$

and

$$i|\dot{\phi}_i\rangle = \hat{P}\left(H_1(t)|\phi_i\rangle + \sum_{jklm}(\rho^{-1})_{ij}\rho^{(2)}_{jklm}\hat{g}_{lm}|\phi_k\rangle\right), \tag{8}$$

with

$$\hat{P} = \hat{\mathbf{1}} - \sum_{j=1}^{M}|\phi_j\rangle\langle\phi_j|, \tag{9}$$

$$\rho_{i,j} = \sum_\sigma\langle\Psi|\hat{a}^\dagger_{i\sigma}\hat{a}_{j\sigma}|\Psi\rangle, \tag{10}$$

$$\rho^{(2)}_{jklm} = \sum_{\sigma\tau}\langle\Psi|\hat{a}^\dagger_{j\sigma}\hat{a}^\dagger_{l\tau}\hat{a}_{m\tau}\hat{a}_{k\sigma}|\Psi\rangle, \tag{11}$$

$$g_{lm}(\mathbf{x}) = \int d\mathbf{x}'\phi^*_l(\mathbf{x}')\frac{1}{|\mathbf{x} - \mathbf{x}'|}\phi_m(\mathbf{x}'), \tag{12}$$

where $\hat{\mathbf{1}}$ denotes the identity operator and $\hat{a}^\dagger_{i\sigma}$ and $\hat{a}_{i\sigma}$ are the Fermion creation and annihilation operators, respectively, associated with spatial orbital i and spin σ. Equation (12) is computed by solving the Poisson equation,

$$\nabla^2 g_{lm}(\mathbf{x}) = -4\pi\phi^*_l(\mathbf{x})\phi_m(\mathbf{x}). \tag{13}$$

It is convenient to rewrite Eq. (8) as

$$i\dot{\phi}_i = \hat{P}[T\phi_i + W_i(t)], \tag{14}$$

where T is kinetic energy.

III. MULTIRESOLUTION CARTESIAN GRID

We discretize spatial orbital functions on a multiresolution Cartesian grid, inspired by the work of Bischoff and Valeev [34] and the finite-volume method [35]. Figure 1(a) schematically shows how to generate it. We start from an equidistant Cartesian grid composed of cubic cells. If a given cell is too large to represent orbital functions with sufficient accuracy, typically near the nuclei, we subdivide it into eight cubic cells with half the side length of the original cell. We continue the subdivision until accuracy requirements are satisfied. The center of each cube is taken as the grid point representing the cell.

The Laplacian $\nabla^2\phi$ of orbital function $\phi(\mathbf{r},t)$ is evaluated at each grid point by finite difference. We first illustrate it for a one-dimensional case for simplicity in Fig. 1(b). One can evaluate the second derivative of a function $f(x)$ at grid point x_i as

$$\frac{d^2}{dx^2}f(x_i) \approx \frac{g_i^+ - g_i^-}{\Delta x_i}, \tag{15}$$

where Δx_i is the size of cell i and the first derivatives $g_i^\pm$ at the cell boundaries are approximated by

$$g_i^+ \approx \frac{2[f(x_{i+1}) - f(x_i)]}{\Delta x_i + \Delta x_{i+1}}, \tag{16}$$

$$g_i^- \approx \frac{2[f(x_i) - f(x_{i-1})]}{\Delta x_i + \Delta x_{i-1}}. \tag{17}$$

We show the extension to two dimensions in Fig. 1(c). The grid points are marked by red and blue circles. In order to evaluate the second derivative with respect to the vertical direction at the center of cell i, we need the first derivative evaluated at the cell boundary marked by the orange triangle, for which we need, in turn, the value of the function at the position marked by the star in cell $i+1$. We approximate this latter by the value $f_{i+1} \equiv f(\mathbf{r}_{i+1})$ at the grid point, i.e., the center of the cell $i+1$. Although inferior in terms of accuracy, this scheme is much more advantageous in terms of computational cost over conventional methods such as the alternating-direction implicit method [36], moving least squares [37,38], and symmetric smoothed particle hydrodynamics [39,40].

Then, in the 3D case, we evaluate the Laplacian $\nabla^2\phi(\mathbf{r})$ as

$$\nabla^2\phi(\mathbf{r}_a) \approx L_{aa}\phi(\mathbf{r}_a) + {\sum_b}' L_{ab}\phi(\mathbf{r}_b), \tag{18}$$

where a and b are cell indices, the primed sum is taken over the cells adjacent to the ath cell, and

$$L_{aa} = -{\sum_b}' L_{ab}, \tag{19}$$

$$L_{ab} = \frac{l_b^2}{l_a^2}\frac{2}{l_a + l_b}\frac{1}{l_a} \quad (a \neq b,\ l_b < l_a), \tag{20}$$

$$L_{ab} = \frac{2}{l_a + l_b}\frac{1}{l_a} \quad (a \neq b,\ l_b \geqslant l_a), \tag{21}$$

with l_a being the side length of the ath cell. If $l_b < l_a$, a face of a cell of side length l_a would contact with l_a^2/l_b^2 adjacent cells of side length l_b. The prefactor l_b^2/l_a^2 of Eq. (20) takes into account the weight of each of the latter.

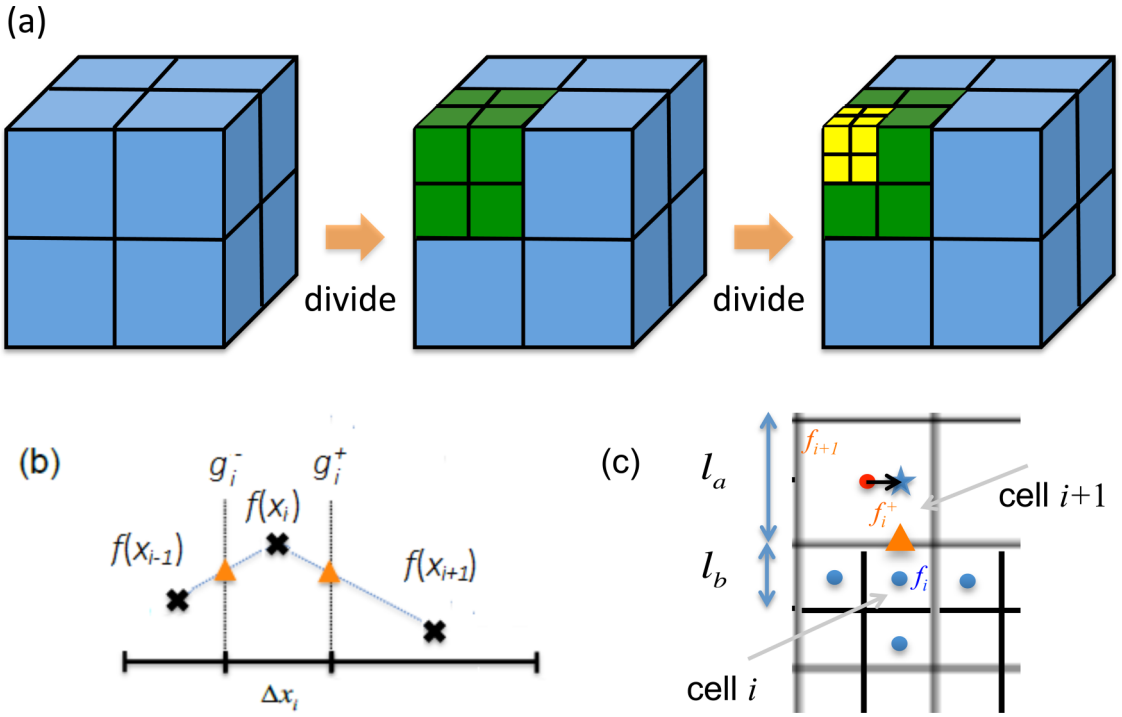

FIG. 1. (a) Schematic of the Cartesian-based multiresolution grids. (b) Schematic of the computation of a second-order differential at one-dimensional irregular grids. (c) Schematic of the computation of the first differential at the surface of the grid at two-dimensional irregular grids. Real grid points are red and blue circles.

IV. NUMERICAL PROCEDURE

We present the essential steps of MCTDHF simulations using a multiresolution Cartesian grid as follows:

Step 1: Generation of grid and Laplacian matrix. We consider a cuboid simulation region V centered at the origin: $\{\mathbf{x} = (x,y,z) \in \mathbb{R}^2 \mid x \in [-x_L,x_L], y \in [-y_L,y_L], z \in [-z_L,z_L], x_L > 0, y_L > 0, z_L > 0\}$. We set the locations of the grid points and prepare the Laplacian matrix elements L_{ab} using Eqs. (19)–(21). These are done only once in the beginning.

Step 2: Computation of ρ and $\rho^{(2)}$. Each time step starts with the computation of ρ and $\rho^{(2)}$, using Eqs. (10) and (11), respectively.

Step 3: Computation of g_{lm}. We solve the Poisson equation (13) to obtain g_{lm} via the conjugate residual method [41,42]. The condition at the simulation boundary ∂V is given by the multipole expansion

$$g_{lm}(\mathbf{x}_{\rm bound}) = \int_V \frac{1}{|\mathbf{x}_{\rm bound} - \mathbf{x}'|}\phi_l^*(\mathbf{x}')\phi_m^*(\mathbf{x}')d\mathbf{x}' \tag{22}$$

$$= \sum_{l=0}^{\infty}\int_V \frac{|\mathbf{x}'|^l P_l(\cos\theta)}{|\mathbf{x}_{\rm bound}|^{l+1}}\phi_l^*(\mathbf{x}')\phi_m^*(\mathbf{x}')d\mathbf{x}' \tag{23}$$

for $\mathbf{x}_{\rm bound} \in \partial V$, where $P_l(z)$ denotes the Legendre polynomial and θ is the angle between $\mathbf{x}'$ and $\mathbf{x}_{\rm bound}$. In the present study, we truncate the sum in Eq. (23) at $l = 2$ (second-order multipole expansion).

Step 4: Time propagation of c_J and ϕ_i. We solve the equations of motion (7) and (14) using a second-order exponential integrator [43,44]. Equation (7) is integrated as

$$c_J^{(1)}(t+\Delta t) = c_J(t) + \Delta t \sum_K \langle J|H|K\rangle c_K, \tag{24}$$

$$c_J^{(2)}(t+\Delta t) = c_J^{(1)}(t+\Delta t) + \Delta t \sum_K \langle J^{(1)}|H|K^{(1)}\rangle c_K^{(1)}(t+\Delta t), \tag{25}$$

$$c_J(t+\Delta t) = \frac{c_J(t) + c_J^{(2)}(t+\Delta t)}{2}, \tag{26}$$

where $|J^{(1)}\rangle$ with superscript (1) denotes the Slater determinant constructed with orbital functions $\phi_i^{(1)}$ defined below in Eq. (27). Equation (14) is integrated as

$$\phi_i^{(1)} = \phi_i(t) + \hat{P}\frac{1}{1 + i\Delta t T/2}[(-i\Delta t T)\phi_i(t) + \Delta t W_i(t)], \tag{27}$$

$$\phi_i^{(2)}(t+\Delta t) = \phi_i^{(1)} + \hat{P}^{(1)}\frac{1}{1+i\Delta t T/2} \times \left[(-i\Delta t T)\phi_i^{(1)} + \Delta t W_i(t+\Delta t)\right], \tag{28}$$

$$\hat{P}^{(1)} = \hat{\mathbf{1}} - \sum_{j=1}^{M} |\phi_j^{(1)}\rangle\langle\phi_j^{(1)}|, \tag{29}$$

$$\phi_i(t+\Delta t) = \frac{\phi_i^{(2)}(t+\Delta t) + \phi_i(t)}{2}. \tag{30}$$

In Eqs. (27) and (28), $(1 + i\Delta t T/2)^{-1}$ is operated by the conjugate residual method [41,42].

Step 5a: Absorbing boundary (only in real-time propagation). To prevent the reflection from the grid boundaries, after each time step, ϕ_i is multiplied by a cosine mask function $M(x,y,z)$ that varies from 1 to 0 between the absorption boundary set at $x = x_0, y = y_0$, and $z = z_0$ ($0 < x_0 < x_L, 0 < y_0 < y_L, 0 < z_0 < z_L$) and the outer boundary ∂V [45,46]:

$$M(x,y,z) = C\left(\frac{|x| - x_0}{x_L - x_0}\right) C\left(\frac{|y| - y_0}{y_L - y_0}\right) C\left(\frac{|z| - z_0}{z_L - z_0}\right), \tag{31}$$

where

$$C(x) = 1 \ \ (x \leqslant 0), \quad \cos(x) \ \ (x > 0). \tag{32}$$

Alternatively, one may use, e.g., exterior complex scaling [47,48].

Step 5b: Rescaling of c_J and orthonormalization of ϕ_i (only in imaginary-time propagation). We obtain the initial ground state via the imaginary-time propagation [49]. After each (imaginary) time step, c_J is rescaled so that $\sum_J |c_J|^2 = 1$, and ϕ_i is orthonormalized through the Gram-Schmidt algorithm.

Step 6: End of time step. We go back to step 2 to start the next time step.

V. EXAMPLES

A. Benchmark: HHG from helium

We simulate the HHG from a helium atom located at the origin. The side length of the cell is set to be 0.6 ($r > 4$), 0.3 ($2 < r < 4$), and $0.15(r < 2)$, respectively, depending on the distance r of the grid point at the center of each cell and the origin. We also set $x_L = 70, y_L = z_L = 35$ and $x_0 = 0.7x_L, y_0 = 0.7y_L, z_0 = 0.7z_L$. The time step size Δt is set to be 0.0025. We consider a laser pulse linearly polarized along the x axis, whose electric field $E(t)$ is given by

$$E(t) = E_{\rm env}(t) \sin \omega t, \tag{33}$$

$$E_{\rm env}(t) = \begin{cases} \omega t/2\pi & (\omega t < 2\pi), \\ 2 - \omega t/2\pi & (2\pi < \omega t < 4\pi), \\ 0 & (\text{otherwise}), \end{cases} \tag{34}$$

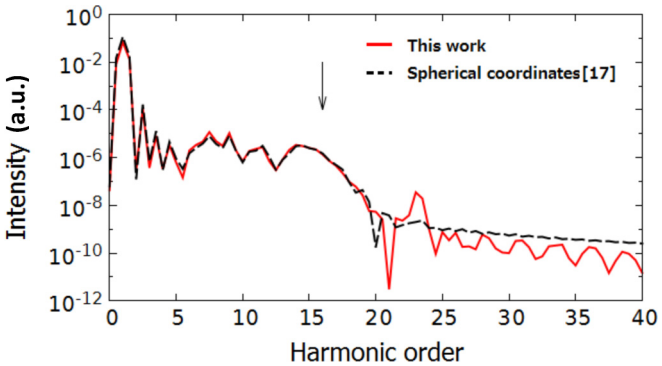

FIG. 2. HHG spectrum of helium computed by multiresolution MCTDHF (red solid line) and method of [17] (black dashed line). The arrow represents the cutoff energy.

with a central wavelength of 400 nm and a peak intensity of 8×10^{14} W/cm^2. For such an ultrashort pulse, the cutoff energy predicted by the semiclassical three-step model [50,51] is $I_p + 2.07U_p = 49.6$ eV, which corresponds to the 16.0th order, where I_p is the ionization potential and U_p is ponderomotive energy. The harmonic spectrum is obtained from the Fourier transform of the dipole acceleration.

In Fig. 2 we compare the HHG spectrum calculated with the present implementation with that calculated with another

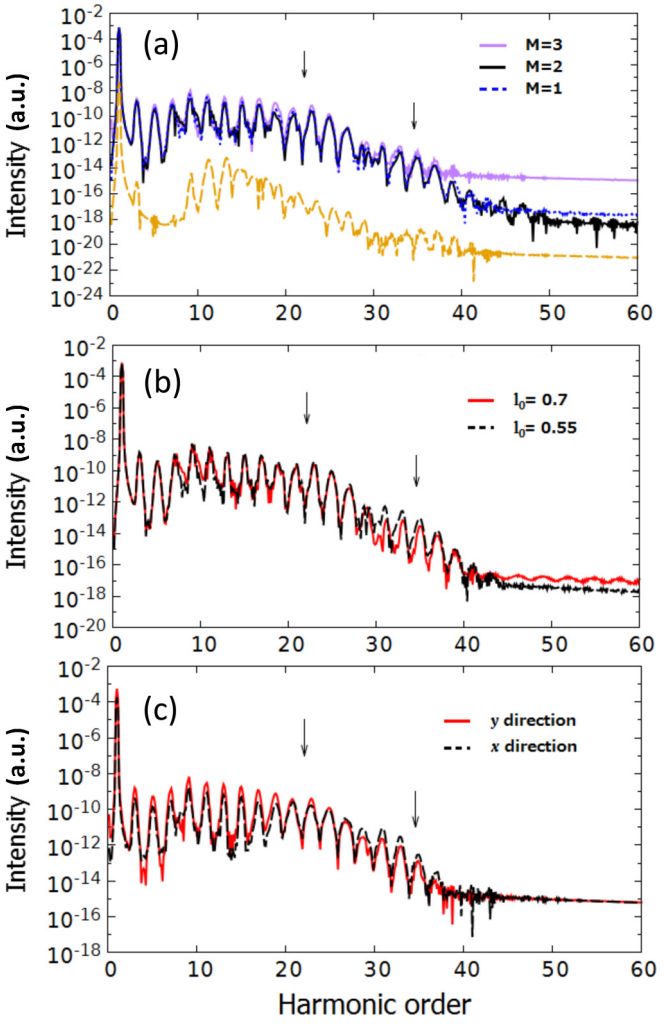

FIG. 3. Calculated high-harmonic spectra from a hydrogen molecule. See text for laser parameters. (a) Comparison of the results with $M = 1$ (blue dotted line), $M = 2$ (black solid line), and $M = 3$ (purple solid line) for laser polarization parallel to the molecular axis. Yellow dashed line: spectrum from H_2^+ multiplied with the ionization probability of H_2 (2.4×10^{-4}). (b) Comparison of the results with $I_0 = 0.7$ (red solid line) and 0.55 (black dashed line). The calculation was done with $M = 1$ for polarization parallel to the molecular axis. (c) Result for laser polarization 30° from the molecular axis [polarization direction is (cos 30°, sin 30°,0)]. $M = 3$ was used. Red solid line: harmonics emitted in the y direction; black dashed line: harmonics emitted in the x direction. Arrows in each panel indicate the cutoff positions expected for H_2 (22.1th order) and H_2^+ (34.6th order).

TABLE I. Ground-state energy (a.u.) of a hydrogen molecule, obtained by relaxation in imaginary time. The values in the column labeled "0.7*" are obtained with grids displaced parallel to the x axis by 0.025 a.u.

Number of	Largest cell side length l_0			
orbitals M	0.7	0.7*	0.6	0.55
1	−1.83661	−1.83622	−1.84318	−1.84123
2	−1.85451	−1.85467	−1.86164	−1.85964
3	−1.86218	−1.86233	−1.86925	−1.86723
6	−1.87329	−1.87342	−1.88027	−1.87756

implementation in spherical coordinates [17]. One can see that they agree with each other very well.

B. HHG from a hydrogen molecule

Next, we simulate the HHG from molecular hydrogen where two hydrogen atoms are located at (±0.7,0,0), respectively. The side length of the cell is set to be l_0 ($r_0 > 4$), $l_0/2$ ($2 < r_0 < 4$), and $l_0/4$ ($r_0 < 2$), respectively, where l_0 is the side length of the largest cells (see Table I for its values). We also set $x_L = y_L = z_L = 27$ and $x_0 = 0.7x_L, y_0 = 0.7y_L, z_0 = 0.7z_L$. The time step size Δt is set to be 0.01.

The ground-state energy, obtained through relaxation in imaginary time, is shown in Table I, where M is the number of orbitals. It consistently tends to the literature value −1.8884 a.u. [52], with an increasing number of orbitals. The slight dependence on M and l_0 has only a small impact on calculated harmonic spectra, as we will see below in Figs. 3(a) and 3(b). The values in the column labeled "0.7*" are obtained with grids displaced parallel to the x axis by 0.025. One can see that the resulting loss of grid symmetry with respect to the yz plane also has only a small impact.

Let us consider a linearly polarized laser pulse with a central wavelength of 800 nm, a peak intensity of 1×10^{14} W/cm^2, and an eight-cycle sine-squared envelope,

$$E(t) = E_0 \sin^2(\omega t/16)\cos(\omega t). \tag{35}$$

Figure 3 presents the HHG spectra for laser polarization parallel to the molecular axis [the x axis; Figs. 3(a) and 3(b)] and 30° from the molecular axis [Fig. 3(c)]. The cutoff energy predicted by the semiclassical three-step model is 34.3 eV, which corresponds to order 22.1. One can see that the simulation is converged with respect to the number of orbitals [Fig. 3(a)] and grid spacing [Fig. 3(b)]. Our multiresolution Cartesian-grid MCTDHF, with no *a priori* assumption of symmetry, can also handle laser polarization oblique to the molecular axis [Fig. 3(c)].

In Fig. 3 we can clearly see the second plateau, somewhat weaker than the first one, extending beyond the cutoff (approximately order 22.1). The second cutoff position is consistent with the value (53.6 eV, or the 34.6th order) predicted by the three-step model with the ionization potential of H_2^+ (34.7 eV). Hence, based on the speculation that the second plateau harmonics are generated from H_2^+ produced via strong-field ionization, we have simulated the HHG from this molecular ion with the same laser parameters. The obtained harmonic spectrum multiplied by the ionization probability of H_2 (2.4×10^{-4}) is plotted as a yellow dashed line in Fig. 3(a).

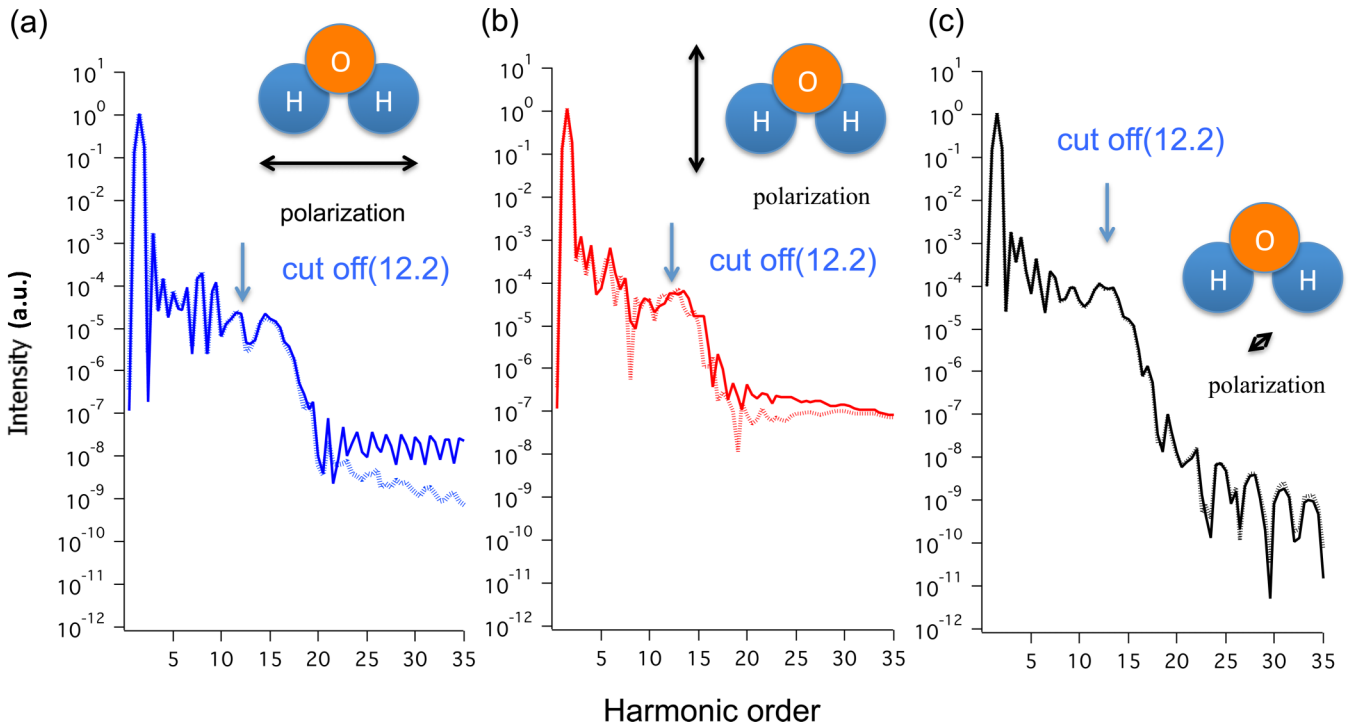

FIG. 4. High-harmonic spectra from a water molecule, calculated with $M = 5$ (dashed) and $M = 6$ (solid), for laser polarization along (a) the x axis (b) the y axis (c) the z axis, as indicated in each panel. Laser polarization in (c) is perpendicular to the plane of the molecule. See text for laser parameters.

The spectrum is much weaker than the second plateau from H_2.

Presumably, the harmonic response from H_2^+ is substantially enhanced by the action of the oscillating dipole formed by the recolliding first electron ejected from the neutral molecule and the neutral ground state. This mechanics is similar to enhancement by an assisting harmonic pulse [53–56], but the enhancement is due to direct Coulomb force from the oscillating dipole, rather than harmonics emitted from it. In the words of the semiclassical three-step model, the recolliding first electron virtually excites H_2^+, facilitating second ionization. Thus, electron-electron interaction plays an important role in high-harmonic generation in some cases (see also [57]), whereas HHG is usually considered a predominantly single-electron process.

C. HHG from a water molecule

As an example of application to molecules of lower symmetry, we simulate the HHG from a water molecule with its oxygen atom located at the origin and two hydrogen atoms at $(\pm 1.4299, 1.10718, 0)$. The side length of the cell is set to be 0.6 ($r_0 > 4$), 0.3 ($2 < r_0 < 4$), and 0.15 ($r_0 < 2$), respectively, where r_0 is the distance from the nearest atom. The outer boundary x_L, y_L, z_L is set to be 60 (axis parallel to the polarization) and 30 (axis perpendicular to the polarization), and the absorption boundary x_0, y_0, z_0 is set to be 0.7 times as long as the outer boundary. The time-step size Δt is set to be 0.0025. We use the same laser pulse shape as in Sec. V A. The cutoff energy predicted by the semiclassical three-step model is 37.3 eV, which corresponds to the 12.0th order.

Figure 4, which presents the harmonic spectra for three different directions of laser polarization, demonstrates the high flexibility of the multiresolution Cartesian-grid MCTDHF implementation. One can see that the curves obtained with $M = 5$ and 6 almost overlap with each other. The simulation with $M = 6$ took ~28 days on a single node with two hexa-core 3.33-GHz Xeon processors. In this case, the computational bottleneck was the solution of Poisson's equation (step 3 in Sec. IV). We expect that the distributed parallelization of the code will substantially reduce the computational time, and the extension to TD-CASSCF [8] and TD-ORMAS [9] methods will further extend the applicability to larger systems.

VI. CONCLUSION

We have numerically implemented the MCTDHF method on a multiresolution Cartesian grid. Whereas previous approaches have relied on the underlying symmetries of the simulated atoms and molecules, the present implementation offers a flexible framework to describe strong-field and attosecond processes of real general molecules. Extension to computationally more compact methods such as TD-CASSCF [8] and TD-ORMAS [9] will be rather straightforward and enable application to large molecules.

As demonstrations, we have successfully calculated high-harmonic spectra from He, H_2, and H_2O. As the presence of the second plateau in Fig. 3 implies, the present implementation will uncover yet unexplored multielectron, multichannel, and multiorbital effects, which only first-principles simulations can reveal.

ACKNOWLEDGMENTS

This work was supported in part by Japan Society for the Promotion of Science (JSPS) KAKENHI Grants No. 25286064, No. 26390076, No. 26600111, and No. 26-10100. This research was also partially supported by the Photon Frontier Network Program of the Ministry of Education, Culture, Sports, Science and Technology (MEXT) of Japan, the Advanced Integration Science Innovation Education and Research Consortium Program of MEXT, the Center of Innovation Program from Japan Science and Technology Agency (JST), and Core Research for Evolutional Science and Technology, Japan Science and Technology Agency (CREST, JST). R.S. gratefully acknowledges support from the Graduate School of Engineering, The University of Tokyo, Doctoral Student Special Incentives Program (SEUT Fellowship).

[1] F. Krausz and M. Ivanov, Rev. Mod. Phys. **81**, 163 (2009).
[2] R. Levis, G. Menkir, and H. Rabitz, Science **292**, 709 (2001).
[3] F. Calegari, D. Ayuso, A. Trabattoni, L. Belshaw, S. D. Camillis, S. Anumula, F. Frassetto, L. Poletto, A. Palacios, P. Decleva, J. B. Greenwood, F. Martín, and M. Nisoli, Science **346**, 336 (2014).
[4] K. Ishikawa and T. Sato, IEEE J. Sel. Top. Quantum Electron. **21**, 8700916 (2015).
[5] T.-T. Nguyen-Dang, M. Peters, S.-M. Wang, and F. Dion, Chem. Phys. **366**, 71 (2009).
[6] T.-T. Nguyen-Dang and J. Viau-Trudel, J. Chem. Phys. **139**, 244102 (2013).
[7] R. P. Miranda, A. J. Fisher, L. Stella, and A. P. Horsfield, J. Chem. Phys. **134**, 244101 (2011).
[8] T. Sato and K. L. Ishikawa, Phys. Rev. A **88**, 023402 (2013).
[9] T. Sato and K. L. Ishikawa, Phys. Rev. A **91**, 023417 (2015).
[10] L. Greenman, P. J. Ho, S. Pabst, E. Kamarchik, D. A. Mazziotti, and R. Santra, Phys. Rev. A **82**, 023406 (2010).
[11] S. Bauch, L. K. Sørensen, and L. B. Madsen, Phys. Rev. A **90**, 062508 (2014).
[12] J. Caillat, J. Zanghellini, M. Kitzler, O. Koch, W. Kreuzer, and A. Scrinzi, Phys. Rev. A **71**, 012712 (2005).
[13] T. Kato and H. Kono, Chem. Phys. Lett. **392**, 533 (2004).
[14] D. J. Haxton and C. W. McCurdy, Phys. Rev. A **91**, 012509 (2015).
[15] H. Miyagi and L. B. Madsen, Phys. Rev. A **87**, 062511 (2013).
[16] D. J. Haxton, K. V. Lawler, and C. W. McCurdy, Phys. Rev. A **86**, 013406 (2012).
[17] T. Sato and K. L. Ishikawa (unpublished).
[18] J. Parker, K. T. Taylor, C. W. Clark, and S. Blodgett-Ford, J. Phys. B **29**, L33 (1996).
[19] E. S. Smyth, J. S. Parker, and K. Taylor, Comput. Phys. Commun. **114**, 1 (1998).
[20] K. L. Ishikawa and K. Midorikawa, Phys. Rev. A **72**, 013407 (2005).

[21] K. L. Ishikawa and K. Ueda, Phys. Rev. Lett. **108**, 033003 (2012).
[22] K. L. Ishikawa and K. Ueda, Appl. Sci. **3**, 189 (2013).
[23] K. Harumiya, I. Kawata, H. Kono, and Y. Fujimura, J. Chem. Phys. **113**, 8953 (2000).
[24] K. Harumiya, H. Kono, Y. Fujimura, I. Kawata, and A. D. Bandrauk, Phys. Rev. A **66**, 043403 (2002).
[25] S. Ohmura, T. Oyamada, T. Kato, H. Kono, and S. Koseki, in *Proceedings of the 12th Asia Pacific Physics Conference (APPC12)*, JPS Conf. Proc. No. 1 (JPS Conference Proceedings, Makuhari, 2014), p. 013087.
[26] S. Ohmura, H. Kono, T. Oyamada, T. Kato, K. Nakai, and S. Koseki, J. Chem. Phys. **141**, 114105 (2014).
[27] X. Guan, K. Bartschat, and B. I. Schneider, Phys. Rev. A **82**, 041404 (2010).
[28] L. Tao, C. W. McCurdy, and T. N. Rescigno, Phys. Rev. A **79**, 012719 (2009).
[29] L. Tao, C. W. McCurdy, and T. N. Rescigno, Phys. Rev. A **80**, 013402 (2009).
[30] L. Tao, C. W. McCurdy, and T. N. Rescigno, Phys. Rev. A **82**, 023423 (2010).
[31] P. A. M. Dirac, Math. Proc. Cambridge Philos. Soc. **26**, 376 (2008).
[32] J. Frenkel, in *Wave Mechanics: Advanced General Theory*, edited by C. Press (Clarendon, Oxford, 1934).
[33] P. Kramer and M. Saraceno, *Geometry of the Time-Dependent Variational Principle* (Springer, Berlin, 1981).
[34] F. A. Bischoff and E. F. Valeev, J. Chem. Phys. **134**, 104104 (2011).
[35] H. Versteeg and W. Malalasekera, *An Introduction to Computational Fluid Dynamics: The Finite Volume Method* (Prentice Hall, Upper side river, 2007).
[36] D. W. Peaceman and J. H. H. Rachford, J. Soc. Ind. Appl. Math. **3**, 28 (1955).
[37] D. Levin, Math. Comput. **67**, 1517 (1998).
[38] C. L. Lopreore and R. E. Wyatt, Phys. Rev. Lett. **82**, 5190 (1999).
[39] R. C. Batra and G. M. Zhang, Comput. Mech. **41**, 527 (2007).
[40] C. L. Tsai, Y. L. Guan, R. C. Batra, D. C. Ohanehi, J. G. Dillard, E. Nicoli, and D. A. Dillard, Comput. Mech. **51**, 19 (2012).
[41] E. Steiefel, Comment. Math. Helvetici **29**, 157 (1955).
[42] Y. Saad, *Iterative Methods for Sparse Linear Systems* (Society for Industrial and Applied Mathematics, Philadelphia, 2003).
[43] S. Cox and P. Matthews, J. Comput. Phys. **176**, 430 (2002).
[44] A. Bandrauk and H. Lu, J. Theor. Comput. Chem. **12**, 1340001 (2013).
[45] J. L. Krause, K. J. Schafer, and K. C. Kulander, Phys. Rev. A **45**, 4998 (1992).
[46] M. Beck, A. Jäckle, G. Worth, and H.-D. Meyer, Phys. Rep. **324**, 1 (2000).
[47] A. Scrinzi and B. Piraux, Phys. Rev. A **58**, 1310 (1998).
[48] A. Scrinzi, Phys. Rev. A **81**, 053845 (2010).
[49] R. Kosloff and H. Tal-Ezer, Chem. Phys. Lett. **127**, 223 (1986).
[50] P. B. Corkum, Phys. Rev. Lett. **71**, 1994 (1993).
[51] K. C. Kulander, K. J. Schafer, and J. L. Krause, in *Super-intense Laser-Atom Physics*, edited by B. Piraux, A. L'Huillier, and K. Rzążewski, NATO ASI Ser. B, Vol. 316 (Plenum, New York, 1993), p. 95.
[52] A. V. Turbiner and N. L. Guevara, Collection of Czechoslovak Chemical Communications **72**, 164 (2007).
[53] K. Ishikawa, Phys. Rev. Lett. **91**, 043002 (2003).
[54] K. L. Ishikawa, Phys. Rev. A **70**, 013412 (2004).
[55] E. J. Takahashi, T. Kanai, K. L. Ishikawa, Y. Nabekawa, and K. Midorikawa, Phys. Rev. Lett. **99**, 053904 (2007).
[56] K. L. Ishikawa, E. J. Takahashi, and K. Midorikawa, Phys. Rev. A **80**, 011807 (2009).
[57] K.-J. Yuan, H. Lu, and A. D. Bandrauk, Phys. Rev. A **92**, 023415 (2015).